

What FIREs Up Star Formation: the Emergence of the Kennicutt-Schmidt Law from Feedback

M. E. Orr^{1*}, C. C. Hayward^{2,3,1}, P. F. Hopkins¹, T. K. Chan⁴,
C.-A. Faucher-Giguère⁵, R. Feldmann⁶, D. Kereš⁴, N. Murray⁷, and E. Quataert⁶

¹TAPIR, Mailcode 350-17, California Institute of Technology, Pasadena, CA 91125, USA

²Center for Computational Astrophysics, Flatiron Institute, 162 Fifth Avenue, New York, NY 10010, USA

³Harvard-Smithsonian Center for Astrophysics, 60 Garden Street, Cambridge, MA 02138, USA

⁴Department of Physics, Center for Astrophysics and Space Science, University of California at San Diego, 9500 Gilman Drive, La Jolla, CA 92093, USA

⁵Department of Physics and Astronomy and CIERA, Northwestern University, 2145 Sheridan Road, Evanston, IL 60208, USA

⁶Department of Astronomy and Theoretical Astrophysics Center, University of California, Berkeley, CA 94720-3411, USA

⁷Canadian Institute for Theoretical Astrophysics, 60 St George Street, University of Toronto, ON M5S 3H8, Canada

Draft date: 10 January 2017

ABSTRACT

We present an analysis of the global and spatially-resolved Kennicutt-Schmidt star formation relation in the FIRE (Feedback In Realistic Environments) suite of cosmological simulations, including halos with $z = 0$ masses ranging from $10^{10} - 10^{13} M_{\odot}$. We show that the Kennicutt-Schmidt (KS) relation emerges robustly due to the effects of feedback on local scales, independent of the particular small-scale star formation prescriptions employed. This is true for the KS relation measured using all of the gas and using only the dense (molecular) gas. We demonstrate that the time-averaged KS relation is relatively independent of redshift and spatial averaging scale, and that the star formation rate surface density is weakly dependent on metallicity ($\propto Z^{1/4}$). Finally, we show that on scales larger than individual giant molecular clouds, the primary condition that determines whether star formation occurs is whether a patch of the galactic disk is thermally Toomre-unstable (not whether it is self-shielding): once a patch can no longer be thermally stabilized against fragmentation, it collapses, becomes self-shielding, cools, and forms stars.

Key words: galaxies: star formation – instabilities – opacity – galaxies: evolution – methods: numerical.

1 INTRODUCTION

Understanding star formation and its effects on galactic scales has been integral to assembling the story of the growth and subsequent evolution of the baryonic components of galaxies. Observationally, the rate at which gas is converted into stars is characterized by the Kennicutt-Schmidt relation, which is a power law correlation between the star formation and gas surface densities in galaxies that holds over several orders of magnitude (Schmidt 1959; Kennicutt 1998; see Kennicutt & Evans 2012 for a recent review).

Numerous studies of the Kennicutt-Schmidt relation have shown that star formation is inefficient on galactic scales, with only a few per cent of a galaxy’s gas mass being converted to stars per galactic free-fall time (Kennicutt 1998; Kennicutt et al. 2007; Daddi et al. 2010; Genzel et al.

2010). Understanding what regulates the efficiency of star formation and results in the observed Kennicutt-Schmidt relation is therefore key to understanding the formation and dynamics of galaxies. Some authors (e.g. Thompson et al. 2005; Murray et al. 2010; Murray 2011; Ostriker & Shetty 2011; Faucher-Giguère et al. 2013; Hayward & Hopkins 2015; Semenov et al. 2016) argue that star formation is *locally* efficient, in the sense that tens of per cent of the mass of a gravitationally bound gas clump within a GMC can be converted into stars on the local free-fall time, and that local stellar feedback processes – including supernovae, radiation pressure, photoheating and stellar winds – must stabilize gas discs against catastrophic gravitational collapse, thereby resulting in the low global star formation efficiencies that are observed. However, others claim that star formation is locally inefficient, with only of order a few per cent of the mass of clumps being converted into stars on a free-fall time

* E-mail: meorr@caltech.edu

independent of their density (Krumholz & Tan 2007; Padoan 1995).

In either scenario, the Kennicutt-Schmidt law is considered to be an emergent relation that holds on galactic scales and results from a complex interplay of the physical processes that trigger star formation and those that regulate it. It has also been argued and observed that the Kennicutt-Schmidt relation breaks down below some length- and time-scales (Onodera et al. 2010; Schruba et al. 2010; Feldmann & Gnedin 2011; Calzetti et al. 2012; Kruijssen & Longmore 2014). Calzetti et al. (2012) found that the Kennicutt-Schmidt relation breaks down due to incomplete sampling of star-forming molecular clouds’ mass function on length scales of less than ~ 1 kpc. Feldmann et al. (2012) claim that this breakdown on sub-kpc scales occurs due to the stochastic nature of star formation itself. Furthermore, Kruijssen & Longmore (2014) argue that the various tracers of gas column density and star formation rate surface density require averaging over some spatial and temporal scales; consequently, when sufficiently small length scales are probed, a tight correlation between the star formation rate surface density and the gas column density should not be observed. Understanding the scales where the Kennicutt-Schmidt law holds therefore informs our theories of star formation as well.

On the length scales where the Kennicutt-Schmidt relation does hold, the canonical power law of the total gas relation is $\Sigma_{\text{SFR}} \propto \Sigma_{\text{gas}}^{1.4}$ with Σ_{SFR} being the star formation rate surface density and Σ_{gas} being the total gas surface density (Kennicutt 1998). However, there has been much debate regarding the power-law index of the relation and its physical origin; the previous literature has found Kennicutt-Schmidt relations ranging from highly sublinear to quadratic (Bigiel et al. 2008; Daddi et al. 2010; Genzel et al. 2010; Feldmann et al. 2011, 2012; Narayanan et al. 2012; Shetty et al. 2013, 2014a,b; Becerra & Escala 2014). Some of the disagreement owes to the particular formulation of the Kennicutt-Schmidt relation considered, such as whether $\Sigma_{\text{HI}+\text{H}_2}$ (total atomic + molecular hydrogen column) or Σ_{H_2} (molecular column alone) is employed (e.g. Rownd & Young 1999; Wong & Blitz 2002; Krumholz & Thompson 2007), with the Σ_{H_2} relation typically having slope ~ 1 . The relation may in principle also depend on the star formation tracer used (e.g. $\text{H}\alpha$, far-infrared, or ultraviolet). Furthermore, there are questions as to whether the index depends on spatial resolution – even on scales larger than the length scale below which the relation fails altogether – or if there are multiple tracks to the Kennicutt-Schmidt relation, each with different slopes across several decades in gas surface density (Ostriker et al. 2010; Liu et al. 2011; Ostriker & Shetty 2011; Feldmann et al. 2011, 2012; Faucher-Giguère et al. 2013).

It has also been suggested that the Kennicutt-Schmidt relation may evolve with redshift or have a metallicity dependence (Bouché et al. 2007; Papadopoulos & Pelupessy 2010; Gnedin & Kravtsov 2011). These are not entirely independent quantities, as metallicity generally increases as galaxies process their gas through generations of stars over cosmic timescales. Because the presence of metals results in more efficient gas cooling, and can thus aid in the transition from diffuse ionized and atomic species to dense molecular gas (Hollenbach & Tielens 1999), Krumholz et al. (2009b) have argued that there is a metallicity-dependent gas surface density cutoff below which the Kennicutt-Schmidt relation

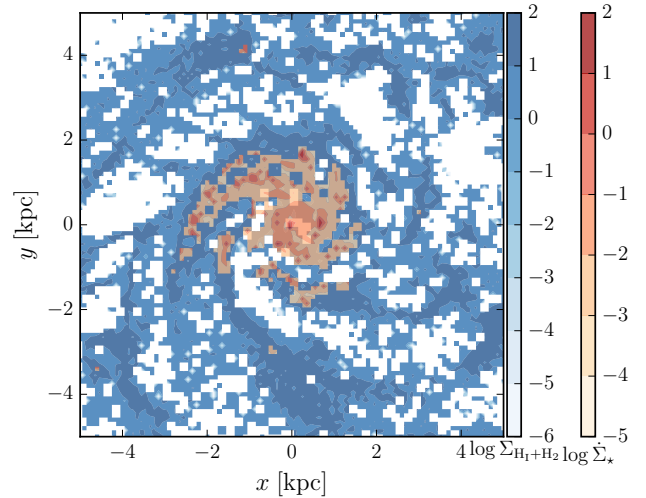


Figure 1. Example of one of our maps, made from a Milky-Way mass simulated galaxy at $z \approx 0$ (galaxy **m12i** from Hopkins et al. 2014), with 100 pc pixels. Neutral hydrogen surface density, $\Sigma_{\text{HI}+\text{H}_2}$ [$\text{M}_\odot \text{pc}^{-2}$] and instantaneous gas star formation rate Σ_* [$\text{M}_\odot \text{yr}^{-1} \text{kpc}^{-2}$] are colored in blues and reds, respectively. Spiral arms and increasing density towards the galactic core are clearly visible, and the instantaneous star formation rate is seen to closely trace the densest gas structures.

becomes steeper owing to the metallicity dependence of the gas column needed to self-shield molecular gas.

Large-volume cosmological simulations often use the Kennicutt-Schmidt law as a sub-grid prescription for star formation, both because of the prohibitive computational complexity of including all of the physics relevant on the scales of star-forming regions, and their inability to resolve even the most-massive giant molecular clouds $\sim 10^6 \text{ M}_\odot$ (e.g. Mihos & Hernquist 1994; Springel & Hernquist 2003). Even idealized disk simulations that have resolution on the order of 100 pc, but are unable to resolve a multiphase ISM, employ star formation prescriptions that assume low star formation efficiencies *a priori* or implement Kennicutt-Schmidt laws indirectly (Schaye & Dalla Vecchia 2008). It has been shown that assuming a power-law star formation relation on the resolution scale can imprint a power-law relation of identical slope on the galactic scale (Gnedin et al. 2014), demonstrating the importance of employing physically motivated sub-grid star formation prescriptions that produce kpc-scale relations with the ‘correct’ slope if the relevant physical processes cannot be treated directly. With advances in computing power, and the ability to execute increasingly complex simulations with more physics at higher mass resolution, simulations have only recently been able to *predict* the Kennicutt-Schmidt relation generically as a result of the physics incorporated in the simulations at the scales of molecular clouds (e.g. Hopkins et al. 2011, 2013a, 2014; Agertz & Kravtsov 2015). Simulations with realistic feedback physics that resolve GMC scales are absolutely critical to understanding the Kennicutt-Schmidt relation due to its emergent nature and the multitude of competing physical effects involved spanning a wide range of scales.

In this paper, we explore the properties and emer-

gence of the Kennicutt-Schmidt relation in the FIRE¹ (Feedback In Realistic Environments) simulations (Hopkins et al. 2014). Specifically, by producing mock observational maps of the spatially-resolved Kennicutt-Schmidt law, we investigate the form of the relation when considering several different tracers of the star formation rate and gas surface densities, and we characterize its dependence on redshift, metallicity, and pixel size. The FIRE simulations are well suited for understanding the physical drivers of the Kennicutt-Schmidt relation as they sample a variety of galactic environments and a large dynamic range in physical quantities (chiefly, gas and star formation rate surface densities), and they directly (albeit approximately) incorporate stellar feedback processes that may be crucial for the emergence of the Kennicutt-Schmidt relation.

2 SIMULATIONS & ANALYSIS METHODS

In the present analysis, we investigate the star formation properties of the FIRE galaxy simulations originally presented in Hopkins et al. (2014), Chan et al. (2015), and Feldmann et al. (2016), which used the Lagrangian gravity + hydrodynamics solver GIZMO (Hopkins 2013) in its pressure-energy smoothed particle hydrodynamics (P-SPH) mode (Hopkins 2013). All of the simulations employ a standard flat Λ CDM cosmology with $h \approx 0.7$, $\Omega_M = 1 - \Omega_\Lambda \approx 0.27$, and $\Omega_b \approx 0.046$. The galaxies in the simulations analyzed in this paper range in $z \approx 0$ halo masses from 9.5×10^9 to $1.4 \times 10^{13} M_\odot$, and minimum baryonic particles masses m_b of 2.6×10^2 to $3.7 \times 10^5 M_\odot$. For all of the simulations, the mass resolution is scaled with the total mass such that the characteristic turbulent Jeans mass is resolved. Consequently, the simulations are able to resolve a multiphase ISM, allowing for meaningful ISM feedback physics. This is crucial because the vast majority of star formation occurs in the most massive GMCs due to the shape of the GMC mass function (Williams & McKee 1997).

The stellar feedback physics implemented in these simulations include approximate treatments of multiple channels of stellar feedback: radiation pressure on dust grains, supernovae (SNe), stellar winds, and photoheating; a detailed description of the stellar feedback model can be found in Hopkins et al. (2014). Star particles in the simulations each represent individual stellar populations, with known ages, metallicities, and masses. Their spectral energy distributions, supernovae rates, stellar wind mechanical luminosities, metal yields, etc. are calculated directly as a function of time using the STARBURST99 (Leitherer et al. 1999) stellar population synthesis models, assuming a Kroupa (2002) IMF.

In these simulations, the galaxy- and kpc-scale star formation efficiency is *not* set by hand. Star formation is restricted to dense, molecular, self-gravitating regions according to several criteria:

- The gas density must be above a critical threshold, $n_{\text{crit}} \sim 50 \text{ cm}^{-3}$ in most runs (and 5 cm^{-3} in those from Feldmann et al. 2016).

- The molecular fraction f_{H_2} is calculated as a function of the local column density and metallicity using the prescription of Krumholz & Gnedin (2011), and the molecular gas density is used to calculate the instantaneous SFR (see below).

- Finally, we identify self-gravitating regions using a sink particle criterion at the resolution scale, specifically requiring $\alpha \equiv \delta v^2 \delta r / G m_{\text{gas}}(< \delta r) < 1$ on the smallest resolved scale around each gas particle (δr being the force softening or smoothing length).

Regions that satisfy all of the above criteria are assumed to have an instantaneous star formation rate of $\dot{\rho}_* = \rho_{\text{mol}}/t_{\text{ff}}$, i.e. 100 percent efficiency per free-fall time. As a large fraction of the dense ($n > n_{\text{crit}}$), molecular ($f_{\text{H}_2} \sim 1$) gas is not gravitationally bound ($\alpha > 1$) at any given time, the *global* star formation efficiency ϵ is less than 100 per cent ($\epsilon < 1$) despite the assumed *local, instantaneous* star formation efficiency per free-fall time being 100 per cent. We will show below that the Kennicutt-Schmidt relation, with its much lower *global, time-averaged* star formation efficiency ($\epsilon \lesssim 0.1$), emerges as a result of stellar feedback preventing dense gas from quickly becoming self-bound and forming stars and disrupting gravitationally bound star-forming clumps on a timescale less than the local free-fall time. We stress here that the emergent Kennicutt-Schmidt relation is *not* a consequence of the star formation prescription employed in the simulations.

In Appendix A we demonstrate this explicitly. We ran several tests restarting one of the standard FIRE simulations with varying physics and star formation prescriptions. For any reasonable set of physics, only variation in the strength of the feedback affected the galactic star formation rates, because the simulated galaxies self-regulate their star formation rates via feedback. A number of independent studies have also shown that once feedback is treated explicitly, the predicted Kennicutt-Schmidt law becomes independent of the resolution-scale star formation criterion (Saitoh et al. 2008; Federrath & Klessen 2012; Hopkins et al. 2012b, 2013c,a,b, 2016; Agertz et al. 2013).

To quantify the spatially resolved Kennicutt-Schmidt relation in the simulations, we analyze data from snapshots spanning redshifts $z = 0 - 6$. The standard FIRE snapshots from Hopkins et al. 2014 and the dwarf runs in Chan et al. (2015) are roughly equipartitioned amongst redshift bins $z \sim 3 - 6$, $2.5 - 1.5$, $1.5 - 0.5$, and < 0.5 , whereas the snapshots of halos from Feldmann et al. (2016) have redshifts evenly spaced between $2 < z < 6$ (these were run to only $z \sim 2$). To compare the snapshots with observational constraints of the Kennicutt-Schmidt relation, we made star formation rate and gas surface density maps of each snapshot's central galaxy. We summed the angular momentum vectors of the star particles in the main halo of each snapshot to determine the galaxy rotation axis and projected along this axis to generate face-on galaxy maps. The projected maps were then binned into square pixels of varying size, ranging from 100 pc to 5 kpc on a side. Only particles within 20 kpc above or below the galaxy along the line of sight were included in the maps (this captures all of the star-forming gas, but excludes distant galaxies projected by chance along the same line-of-sight in the cosmological box). An example of the resulting maps can be found in Figure

¹ <http://fire.northwestern.edu>

1, which shows maps of the gas surface density and the instantaneous star formation rate surface density in the **m12i** simulation from Hopkins et al. (2014), at redshift $z \approx 0$ with 100 pc pixels.

Using the star particle ages, we calculated star formation rates averaged over the previous 10 and 100 Myr, correcting for mass loss from stellar winds and other evolutionary effects as predicted by STARBURST99 (Leitherer et al. 1999). We also considered the instantaneous star formation rate of the gas particles (defined above). A time-averaging interval of 10 Myr was chosen because this approximately corresponds to the timescale traced by recombination lines such as H α , whereas UV and FIR emission traces star formation over roughly the past 100 Myr (e.g. Kennicutt & Evans 2012).² The instantaneous star formation rate of the gas particles covers a larger range of star formation rates because it is not constrained at the low end directly by the mass resolution of our simulations; it is a continuous quantity intrinsic to the gas particles themselves. This quantity best demonstrates the direct consequences of feedback on the gas *in situ* by locally tracing the star formation rate, whereas the other two SFR tracers are more analogous to observables.

The gas surface density tracers were also chosen on the basis of observable analogues, including all gas, neutral hydrogen gas (total HI + H₂ column, accounting for metallicity and He corrected), and “Cold & Dense” gas which we specifically define here and throughout this paper as gas with $T < 300$ K and $n_{\text{H}} > 10 \text{ cm}^{-3}$. These roughly correspond to the total gas, atomic + molecular gas (HI + H₂), and cold molecular gas reservoirs observed in galaxies. We have checked that the approximation for the molecular gas component ($T < 300$ K, $n_{\text{H}} > 10 \text{ cm}^{-3}$) yields molecular gas fractions similar to the molecular fraction f_{H_2} calculated in GIZMO itself. We have opted to use the aforementioned approximation rather than reconstruct the f_{H_2} predicted by the Krumholz & Gnedin (2011) model (which not output in the snapshots) as the f_{H_2} model assumes a simplified geometry at the resolution scale, that can get the local optical depth quite wrong,³ and a more detailed analysis of the true molecular fraction of the gas would require a careful radiative transfer post-processing, which we leave to a later work. We acknowledge that because of the rather strict density and temperature criteria, and the lack of any consideration to the local UV field or the geometry of the gas, we may underestimate the molecular gas column by up to a factor of a few.

Other quantities are calculated as the mass-average in

each pixel, including the gas metallicity⁴ Z , the Keplerian velocity v_c , and the dynamical angular velocity Ω , defined here as

$$\Omega = \frac{v_c}{R} = \frac{(GM(< R))^{1/2}}{R^{3/2}}, \quad (1)$$

where R is the galactocentric radius of the pixel and $M(< R)$ is the total mass enclosed within that radius (and G is the gravitational constant). These quantities allow us to investigate the dependence of star formation on gas phase metallicity, approximate the optical depth of star-forming regions, and relate galactic dynamical times to star-forming regions.

In our analysis we treat pixels from all simulations and all times equally, unless otherwise stated. However we wish to ensure that only well-resolved pixels contribute. Recalling that each of our simulations has a fixed baryonic particle mass, m_b , we discard pixels which contain < 3 gas particles; for a pixel size l , this means only gas surface densities $\Sigma_{\text{gas}} > 3 \times 10^{-3} \text{ M}_{\odot} \text{ pc}^{-2} (m_b/1000 \text{ M}_{\odot}) (l/\text{kpc})^{-2}$ will be considered. However, in the example above ($m_b \sim 1000 \text{ M}_{\odot}$, $l \sim \text{kpc}$), the observed Kennicutt (1998) relation gives a typical star formation surface density $\Sigma_{\text{SFR}} \sim 10^{-7} \text{ M}_{\odot} \text{ yr}^{-1} \text{ kpc}^{-2}$ at this minimum Σ_{gas} , so in ~ 10 Myr, the expected number of $m_b \sim 1000 \text{ M}_{\odot}$ star particles formed will be just 0.001. Obviously, the distribution of star formation rates will not, then, be resolved (even if the simulations capture the mean star formation rate correctly, the discrete nature of star formation means only 1 in 1000 pixels will have a star particle, while 999 have none). We therefore adopt a more appropriate criterion: (1) we first calculate the *mean* Σ_{SFR} per pixel from each simulation, for all their pixels with a given number of gas particles (fixed Σ_{gas}); (2) we estimate the average number $\langle N_{\star}(\Delta t) \rangle$ of star particles this would produce in the time Δt (10 or 100 Myr, as appropriate); (3) if this is $< 1 (= N_{\text{min},\star})$, we discard all pixels which contain this number or fewer gas particles. For the example above, for $\Delta t = 10$ Myr (100 Myr), this requires > 500 (> 100) gas particles per pixel for a “resolved” star formation rate. We have repeated this exercise using instead the observed Kennicutt-Schmidt relation (instead of the predicted one), to estimate the resolved thresholds, and find it gives nearly identical results. We have also verified that changing the threshold $N_{\text{min},\star}$ by an order of magnitude in either direction does not change any of our conclusions here; we note too that the *average* star formation rates from low-resolution simulations continue to agree well with our higher-resolution simulations down to $\langle N_{\star}(\Delta t) \rangle$ as low as ~ 0.001 .

Comparing with observations, we compiled the resolved Kennicutt-Schmidt observations from a large number of papers at various resolution scales commensurate with our mock observational maps (Kennicutt 1998; Kennicutt et al. 2007; Bigiel et al. 2008; Genzel et al. 2010; Bothwell et al. 2010; Onodera et al. 2010; Verley et al. 2010; Shapiro et al. 2010; Wei et al. 2010; Daddi et al. 2010; Shi et al. 2011; Lisenfeld et al. 2011; Boquien et al. 2011; Tacconi et al. 2013; Freundlich et al. 2013). We then represent the range of the compiled data with shaded contours, including the ex-

² Directly computing SFR indicators from the simulations (e.g. Hayward et al. 2014; Sparre et al. 2015) rather than computing the SFR averaged over the past 10 or 100 Myr would provide a more accurate comparison with the observed Kennicutt-Schmidt relation, but doing so would considerably expand the scope of this work, so we leave it to a future study.

³ For the purposes of our star formation criteria, however, this is for the vast majority of cases not an issue. Due to the steepness of the exponential attenuation of the local UV field, we care only whether, strictly speaking, the gas is optically thin or thick. Not necessarily *how* thin or thick, as any optical depth $\tau \gg 1$ effectively yields $\exp(-\tau) \ll 1$, and $\tau \ll 1$ similarly yields $\exp(-\tau) \approx 1$.

⁴ In this paper, we take solar metallicity to be $Z_{\odot} \approx 0.0142$ when scaling metallicities (Asplund et al. 2009).

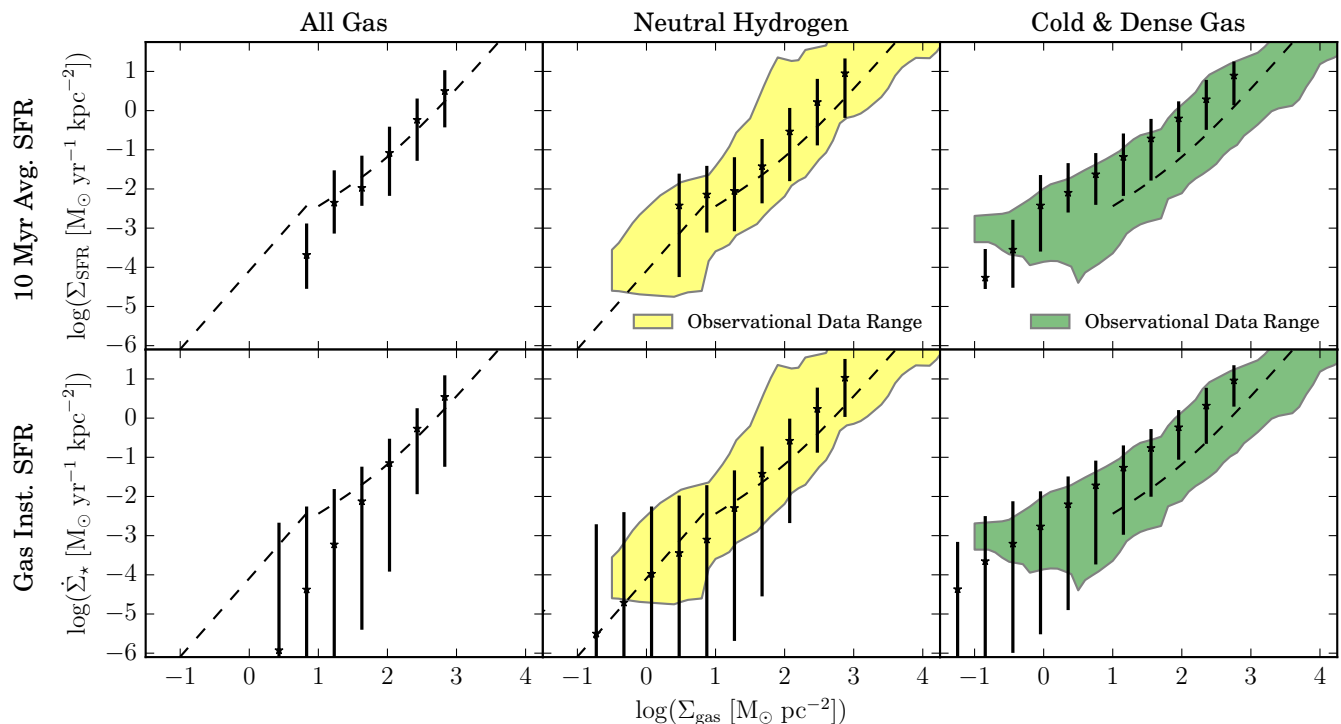


Figure 2. Kennicutt-Schmidt relation in the FIRE runs in 1 kpc^2 pixels, binned by Σ_{gas} , for several gas and star formation “tracers”. Neutral (and molecular) hydrogen is $\sim \Sigma_{\text{HI}+\text{H}_2}$, and Cold & Dense gas includes particles with $T < 300 \text{ K}$ and $n_{\text{H}} > 10 \text{ cm}^{-3}$ ($\sim \Sigma_{\text{H}_2}$). The gas instantaneous star formation rate is calculated directly from the gas particles in each pixel, whereas the 10 Myr average star formation rate is calculated from the young star particles in each pixel. Linear average values of the pixel distribution are plotted in bins of gas surface density, with error bars denoting the 5-95% range of resolved star formation in the bins. The yellow and green shaded regions denote the observational data range from the studies enumerated in §2. The star formation relations derived in §4.1 and §4.2 are plotted with dashed black lines, using the fiducial values assumed there and $\Sigma_{\star} = 10^2 \text{ M}_{\odot} \text{ pc}^{-2}$. The simulations robustly reproduce a resolved Kennicutt-Schmidt relation in broad agreement with observations, regardless of the particular star formation or gas tracer considered.

tent of the star formation distributions (determined by eye) for two tracers of gas surface density ($\Sigma_{\text{HI}+\text{H}_2}$ and Σ_{H_2}). No distinction is made between the many estimators of star formation rate used in the aforementioned papers; they are taken at face value.

3 KENNICUTT-SCHMIDT RELATION IN THE SIMULATIONS

3.1 Dependence of the Kennicutt-Schmidt Relation on Star Formation and Gas Tracers

Figure 2 demonstrates the broad emergence of the Kennicutt-Schmidt power law relation, irrespective of specific choice of star formation or gas tracer, in the FIRE simulations. Two of our star formation rate tracers, the 10 Myr-averaged and gas instantaneous star formation rates, yield very similar Kennicutt-Schmidt relations. The points denote the linear average of the star formation rate distribution. The error bars in Figure 2 denote the 5% to 95% inclusion interval in the distribution of the star formation rates of pixels in that bin of gas surface density.

More restrictive gas tracers (e.g. taking gas with $T < 300 \text{ K}$ and $n_{\text{H}} > 10 \text{ cm}^{-3}$ instead of all neutral hydrogen gas) yield shallower power-law slopes. This is intuitive because by placing more restrictions on the gas column, we

are taking pixels at a given star formation rate and moving them to lower gas surface densities (to the left) by reducing what gas contributes to the overall gas column density. The restrictions are non-linear: at high surface densities, the gas is predominately molecular, and added restrictions do little to change the participating gas column, whereas at low surface densities, relatively little of the gas column may remain after making these additional cuts. Little difference is seen between the star formation distributions in $\Sigma_{\text{SFR}} - \Sigma_{\text{gas}}$ space when considering the surface densities of all gas versus neutral gas (first and second columns of Figure 2) because the contribution of ionized gas to the total gas column is small in regions where significant star formation is occurring. In contrast, there is a marked change in slope of the Kennicutt-Schmidt relation when moving from the surface density of neutral hydrogen gas to that of Cold & Dense gas ($T < 300 \text{ K}$, $n_{\text{H}} > 10 \text{ cm}^{-3}$), with the slope shifting from ~ 1.7 to ~ 1.2 for the gas instantaneous star formation rate. This is due to the fact that significant amounts of star formation can occur in “small” pockets of molecular gas, relative to the overall gas column, yielding a shallower slope than when considering neutral gas.

Broadly speaking, all of our various formulations of the Kennicutt-Schmidt relation in the FIRE simulations agree with the corresponding spatially resolved observational data, as represented by the shaded regions in the panels of Figure 2. There is some offset between the sim-

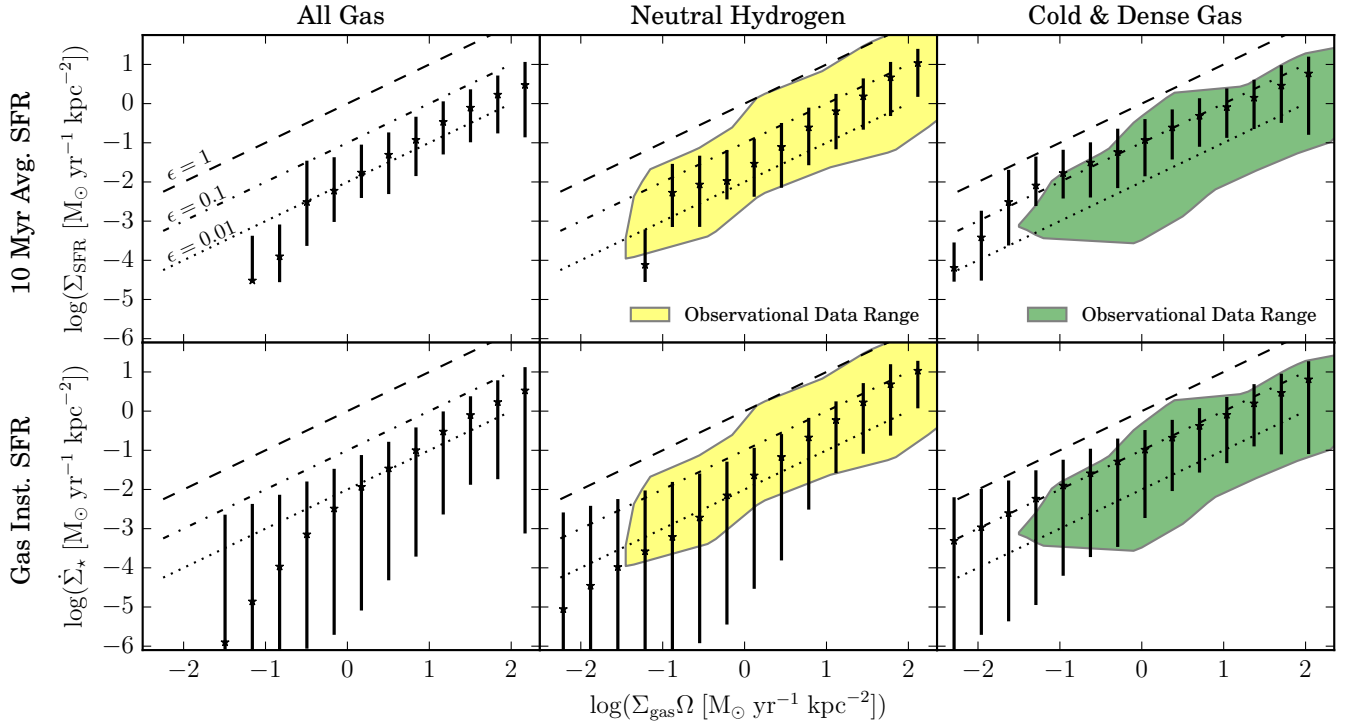


Figure 3. Elmegreen-Silk relation in the FIRE runs in 1 kpc² pixels, in the style of Figure 2. Lines of constant star forming efficiency are plotted, with $\epsilon = (0.01 - 1)$. The simulated galaxies have kpc-scale star formation efficiencies increasing from $\sim 1\%$ (all gas) to $\sim 10\%$ (Cold & Dense gas) as denser gas tracers are selected.

ulations and observations for our Cold & Dense gas surface density, which may indicate that our approximation underestimates the true molecular gas column, but they agree in form with the observed range of molecular gas data. Moreover, the distribution of star formation rates in the FIRE simulations overlap with the Damped Ly α Systems (DLAs) observed at high redshift by Rafelski et al. (2016). Though we appear to see analogues to these systems at 1 kpc² pixel sizes, we leave it to a future work to investigate the detailed physical properties of these systems.

3.1.1 Elmegreen-Silk Relation (Alternative KS Law)

Alternatively, in Figure 3, we probe the global efficiency of gas turning into stars in a dynamical time according to

$$\dot{\Sigma}_* = \epsilon \Sigma_{\text{gas}} \Omega, \quad (2)$$

where ϵ represents the “star formation efficiency” on kpc scales; this relation is known as the Elmegreen-Silk relation (Elmegreen 1997; Silk 1997). For both the neutral hydrogen and Cold & Dense gas surface densities for which we have observations to compare with (where ϵ ranges between $10^{-3} - 1$), we see systematic agreement. We find kpc-averaged star formation efficiencies of $\epsilon \sim 0.01 - 0.1$ consistently for our entire range of star formation rate surface density. Dashed black lines indicate constant efficiencies between 0.01 and 1. Without feedback, one would expect to see $\epsilon \sim 1$.

3.1.2 100 Myr Averaged Star Formation Rate

In Figure 4, we see a clear flattening of the 100 Myr-averaged star formation rate surface density relative to the 10 Myr average, for both neutral hydrogen and molecular gas columns at low gas surface densities, $\Sigma_{\text{gas}} \lesssim 1 \text{ M}_{\odot} \text{ pc}^{-2}$. This is ascribable to effects discussed in §3.2 and §3.4, where individual or small numbers of young star particles are scattered into regions of very low gas surface density that are not actually forming stars. Moreover, dynamical changes in star-forming regions over the averaging period (100 Myr) cause gas complexes to dissipate and produce small numbers of star particles left in now-diffuse galactic environments. At high gas columns, $\Sigma_{\text{gas}} > 10 \text{ M}_{\odot} \text{ pc}^{-2}$, the 100 Myr average star formation rate surface densities agree well with the shorter time-scale estimators.

3.2 Pixel Size Dependence

The Kennicutt-Schmidt relation that we find in the FIRE simulations does not appear to have a significant dependence on pixel size (i.e. map resolution) for pixels with sufficiently resolved gas and star formation rate tracers (\gtrsim few gas/star particles per pixel), as shown in Figure 5. Over the range of pixel sizes we investigate, 100 pc - 5 kpc (0.01 - 25 kpc²), the slope of the power law varies only weakly between ~ 1 and $\sim 4/3$. At the low end of the relation in Σ_{gas} , we expect the scatter to grow as Poisson statistics become important when only a few star particles are present in the pixels on average. However, because we exclude poorly-sampled pixels, this simply manifests as a lower limit to the plotted Σ_{gas} for smaller pixels sizes (c.f. §2).

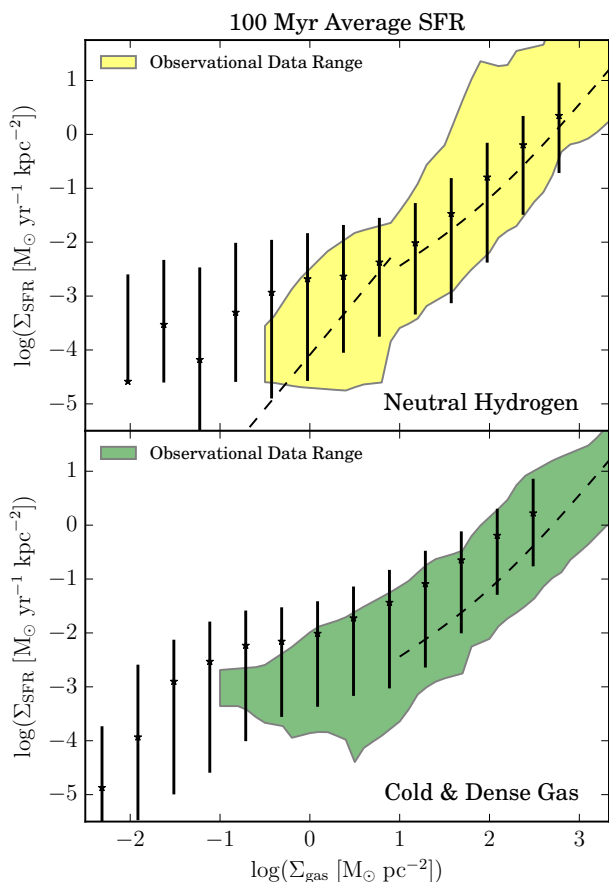


Figure 4. Kennicutt-Schmidt relation for the 100 Myr-averaged star formation rate in 1 kpc^2 pixels, as Figure 2. The “observed” contours are those measured with $\sim 10 \text{ Myr}$ tracers in Figure 2. At high Σ_{gas} , the ~ 10 and $\sim 100 \text{ Myr}$ estimators agree well. At low Σ_{gas} , the Σ_{SFR} from the $\sim 100 \text{ Myr}$ tracer flattens. This appears to stem from a breakdown in the correlation between 100 Myr-old stars and the observed gas tracers, either from migration or other dynamical effects (e.g. mergers or strong outflow events).

Broadly, our results are in agreement with observations at various pixel sizes, in spite of our likely systematic underestimation of column density in our “molecular” (Cold & Dense) gas. However, given our mass resolution, at our smallest pixel size (100 pc), none of our simulations are able to adequately sample star formation at gas surface densities $\lesssim 10 \text{ M}_\odot \text{ pc}^{-2}$, where observations exhibit the largest scatter. At least three processes cause the correlation of the star forming gas and young star particles to break down on scales less than $l \sim 500 \text{ pc}$. (1) The relative velocities between star forming gas and the young stars they produce cause them to wander into different pixels, thus they become uncorrelated on a pixel-by-pixel basis, when $v_p \sim l/\Delta t$. For 100 pc pixels and 100 Myr time bins, this is a relative velocity of only $\sim 1 \text{ km s}^{-1}$ (10 km s^{-1} for $\Delta t \sim 10^7 \text{ yr}$), so we would expect significant scatter to arise from this effect at the smallest pixel sizes. (2) Dynamical processes affecting gas and star particles, like dispersion of GMCs, major mergers, or SNe, over the time bin (i.e. $10 - 100 \text{ Myr}$) cause greater fluctuations from the power law average as pixel size decreases. (3) When considering small ($< 1 \text{ kpc}$) pixels, scatter is caused

by the stochastic nature of the star formation in the simulations.

3.3 Redshift Independence

We find no significant redshift dependence of the Kennicutt-Schmidt relation of the FIRE galaxies. The relation’s insensitivity to redshift in the simulations can be seen in the top panel of Figure 6, where the snapshots are colored by redshift bin ($z < 0.5$, $0.5 - 1.5$, $1.5 - 2.5$, $3 - 6$), and the 10 Myr -averaged Σ_{SFR} and neutral gas surface density are considered. Some scatter is seen in the average values between redshift bins, but any dependence on redshift is much smaller than the range of the data itself. The absence of any redshift dependence persists for all measures of star formation rate. Though the absolute amount of star formation varies with redshift, the correlation between gas column and star formation rate surface density remains consistent.

3.4 Metallicity Dependence

We see in the bottom panel of Figure 6 evidence of a weak dependence on metallicity for the Kennicutt-Schmidt relation in the FIRE runs. For all gas surface densities, more metal-rich gas exhibits elevated star formation rates, with an admittedly large scatter. Interestingly, none of our forms of the Kennicutt-Schmidt law exhibit a notable metallicity-dependent cutoff in star formation, as some models predict (Krumholz et al. 2009b). For our 10 and 100 Myr-averaged star formation rates, this may be an issue of adequately sampling star formation rates in the “cutoff” regime of $\dot{\Sigma}_* \sim 10^{-(3-4)} \text{ M}_\odot \text{ yr}^{-1} \text{ kpc}^{-2}$. However, for the well-resolved instantaneous star formation rate, the form of the star formation relation does not change at all for any of the metallicity bins in the “cutoff” regime that Krumholz et al. (2009b) find. The instantaneous star formation rate tracer, as with the averaged star formation rate tracers, presents higher star formation rates for metal-enriched gas even at these low gas surface densities, but the change is smooth, rather than a “threshold” effect.

Figure 7 illustrates the strength of the metallicity dependence. Binning pixels by gas surface density Σ_{gas} and normalizing by the average star formation rate in each Σ_{gas} bin, we find that star formation rate surface density increases weakly with metallicity, across all Σ_{gas} . This presentation of the data normalizes out the Σ_{gas} dependence to highlight the much weaker Z dependence. A by-eye fit of a power law with slope $1/4$ is plotted as a dashed black line. This slope is much shallower than the slope derived in §4.2 but on the order of the predicted metallicity dependence of SNe feedback’s momentum injection (ranging from $\sim 1/10 - 3/14$; Cioffi et al. 1988; Martizzi et al. 2015)⁵.

⁵ As described in Hopkins et al. (2014), when SNe explode in regions such that their cooling radii will be unresolved (common in the lower-resolution simulations here with particle masses $\gtrsim 10^4 \text{ M}_\odot$), the ejecta are assigned a terminal momentum based on the detailed individual explosion models from Cioffi et al. (1988), which scale as $p_t \propto Z^{3/14}$. However, the metallicity dependence in Figure 7 persists if we restrict only to our highest-resolution simulations.

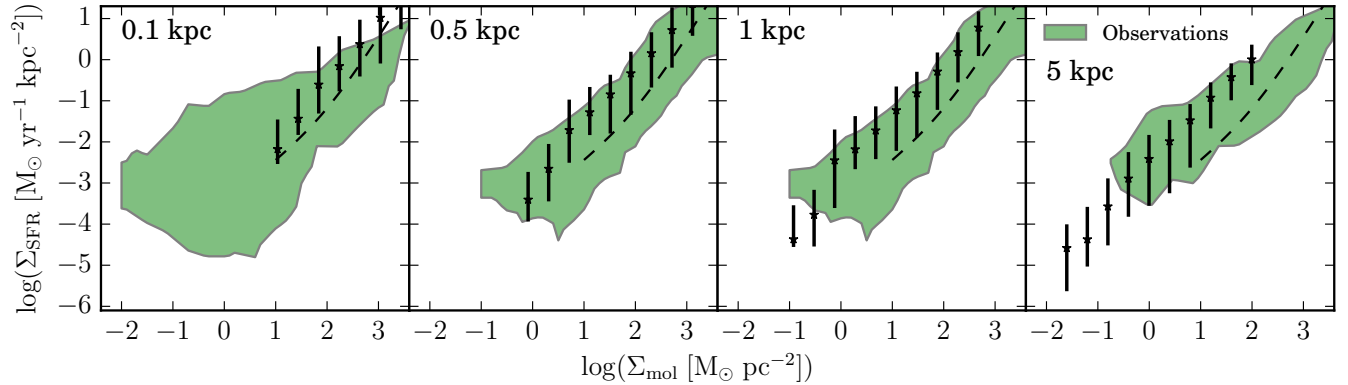


Figure 5. Pixel size dependence of the Kennicutt-Schmidt relation in the FIRE simulations. Σ_{mol} is the surface density of Cold & Dense gas ($T < 300$ K, $n_{\text{H}} > 10 \text{ cm}^{-3}$); Σ_{SFR} is the 10 Myr averaged star formation rate surface density. Plotted points and error bars are as in Figure 2. Green regions denotes observations at appropriate resolution for comparison from papers enumerated in §2, with the 1 kpc observations used for both 500 pc and 1 kpc, as a number of the source observations lie between those two resolutions. Star formation relations derived in §4.1 are plotted with dashed black lines using the fiducial values assumed there and $\Sigma_{\star} = 10^2 \text{ M}_{\odot} \text{ pc}^{-2}$. For each pixel size, there is a threshold in Σ_{mol} below which star formation is poorly resolved given even our highest mass resolution, as described in §2. Above this threshold, the simulated galaxies’ KS relation exhibits no systematic trend with pixel size despite dynamical processes that might be expected to break down the correlations between young stars and gas on small scales (prominent at small pixels sizes).

Though the scatter within bins is quite large, this weak dependence is rather robust.

4 PHYSICAL INTERPRETATION

On the scales of tens or hundreds of millions of years, it is possible to understand star formation as an equilibrium process (on galactic scales) in which the inputs of either momentum injection from stellar feedback (at high gas surface density) or energy from photoheating (at low gas surface density) balance gravitational collapse.

4.1 High Gas Surface Density Regime

In our analysis, there is a marked transition in the star formation rate distribution at gas column densities above $\Sigma_{\text{gas}} \sim 100 \text{ M}_{\odot} \text{ pc}^{-2}$. Above this threshold, almost all the gas forms stars on or very near the Kennicutt-Schmidt power law. Here, supernova feedback becomes an increasingly important mechanism for injecting momentum into the ISM, as the massive young stars produced are embedded in dense molecular environments to which they can effectively couple.

A star formation relation can be derived considering the limit wherein the ISM is supported against collapse by turbulent pressure (Ostriker & Shetty 2011; Faucher-Giguère et al. 2013; Hayward & Hopkins 2015; Torrey et al. 2016). Here, stellar feedback injects momentum into the ISM at a rate per area proportional to $\dot{\Sigma}_{\star}(P_{\star}/m_{\star})$, where (P_{\star}/m_{\star}) is the characteristic momentum injected per mass of young stars formed, and is dissipated in the mass of nearby gas per area Σ_{gas} on some characteristic timescale related to the coherence time of the turbulent eddies t_{eddy} , where $t_{\text{eddy}} \sim l_{\text{eddy}}/\sigma_{\text{eddy}}$, l_{eddy} being the spatial scale of the eddy and σ_{eddy} the turbulent velocity σ_{T} . As we are considering an approximately disk-like environment for star formation in the high gas surface density regime, the largest eddies will likely have length scales on the order of the disk scale height H (Martizzi et al. 2016), so $l_{\text{eddy}} \sim H \sim \sigma_{\text{T}}/\Omega$,

with σ_{T} being the turbulent velocity and Ω being the local orbital dynamical frequency. We are concerned with the largest eddies, which contain most of the turbulent energy. Hence, the timescales of turbulent energy dissipation scale as $t_{\text{eddy}} \approx t_{\text{diss}} \sim H/\sigma_{\text{T}} \sim \Omega^{-1}$. Equating these rates of turbulent momentum injection and momentum dissipation in gas, we find,

$$\dot{\Sigma}_{\star}(P_{\star}/m_{\star}) \approx \sigma_{\text{T}}\Sigma_{\text{gas}}/t_{\text{diss}}, \quad (3)$$

substituting in our relations, this yields a star formation rate of,

$$\dot{\Sigma}_{\star} \approx \sigma_{\text{T}}\Omega\Sigma_{\text{gas}}\left(\frac{P_{\star}}{m_{\star}}\right)^{-1}. \quad (4)$$

Relating $\sigma_{\text{T}}\Omega$ back to the disk surface density with a modified Toomre- Q parameter (Toomre 1964),

$$Q = \frac{\kappa\sqrt{c_s^2 + \sigma_{\text{T}}^2}}{\pi G\Sigma_{\text{disk}}}, \quad (5)$$

where κ is the epicyclic frequency $\sim \sqrt{2}\Omega$ for galactic potentials, c_s is the sound speed, $\Sigma_{\text{disk}} \approx \Sigma_{\text{gas}} + \Sigma_{\star}$ is the disk surface density. Here we include the self-gravity contribution from the collisionless stellar component of the disk, which is correct up to some order unity prefactor. Assuming that we are turbulently rather than thermally supported, $\sqrt{c_s^2 + \sigma_{\text{T}}^2} \approx \sigma_{\text{T}}$. Substituting this in we find,

$$\dot{\Sigma}_{\star} \approx \frac{\pi}{\sqrt{2}}GQ\left(\frac{P_{\star}}{m_{\star}}\right)^{-1}\Sigma_{\text{gas}}(\Sigma_{\text{gas}} + \Sigma_{\star}). \quad (6)$$

Adopting a fiducial value for (P_{\star}/m_{\star}) of $\sim 3000 \text{ km s}^{-1}$ (e.g. Ostriker & Shetty 2011; Faucher-Giguère et al. 2013; Kim & Ostriker 2015; Martizzi et al. 2015), this yields

$$\dot{\Sigma}_{\star} \approx 3.3 \times 10^{-2} \left(\frac{P_{\star}/m_{\star}}{3000 \text{ km/s}}\right)^{-1} \left(\frac{\Sigma_{\text{gas}}(\Sigma_{\text{gas}} + \Sigma_{\star})}{10^4 \text{ M}_{\odot}^2 \text{ pc}^{-4}}\right) Q \text{ M}_{\odot} \text{ yr}^{-1} \text{ kpc}^{-2}. \quad (7)$$

For the gas-dominated regime, where $\Sigma_{\text{gas}} \gg \Sigma_{\star}$, we recover a quadratic relation for star formation. Similarly,

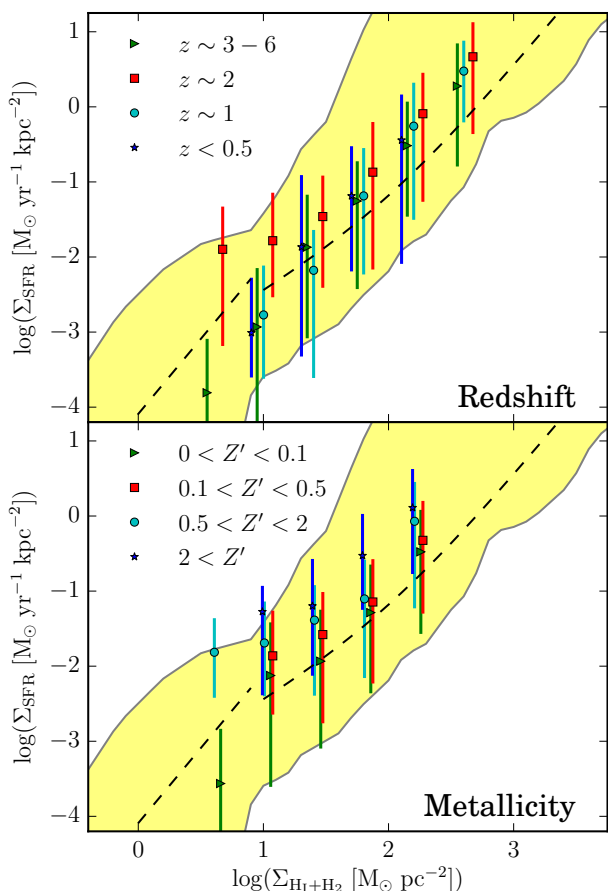


Figure 6. Kennicutt-Schmidt relation binned in redshift and metallicity at 1 kpc^2 pixel size. In both panels, within their respective redshift and metallicity bins, average values of the 10 Myr average Σ_{SFR} are plotted in bins of $\Sigma_{\text{HI}+\text{H}_2}$, in the style of Figure 2. Yellow region denotes appropriate observations and dotted lines derived star formation relations, as in Figure 2. **Top Panel:** Simulation snapshots binned by redshift, with markers denoting different epochs. No significant dependence on redshift is seen – the range of data in each bin is greater than any systematic difference between them. **Bottom Panel:** Pixels from snapshots binned by gas metallicity, with markers indicating intervals in $Z' = Z_{\text{gas}}/Z_{\odot}$. Though weak compared to data range in each bin, a metallicity dependence of Σ_{SFR} is seen at all $\Sigma_{\text{HI}+\text{H}_2}$. No metallicity-dependent cutoff is evident.

should the stellar component dominate, as may be the case in stellar systems with older populations, a law linear in Σ_{gas} is found; this appears to be in good agreement with the slope of the Kennicutt-Schmidt relation seen in the FIRE runs.

The observed weak metallicity dependence seen in Figures 6 & 7, combined with the result shown in the lower left panel of Figure A1, which shows explicitly that the star formation rate varies with the strength of feedback, can be partly explained by a weak dependence of the final momentum injection from SNe feedback on the metallicity of the surrounding gas, e.g. $(P_{\star}/m_{\star})^{-1} \sim Z^{0.114}$ (Martizzi et al. 2015).

The Kennicutt-Schmidt relation predicted by a turbulence-supported model assuming that the stellar surface density $\Sigma_{\star} \gg \Sigma_{\text{gas}}$, with its approximately linear power-law slope, agrees remarkably well with the Kennicutt-

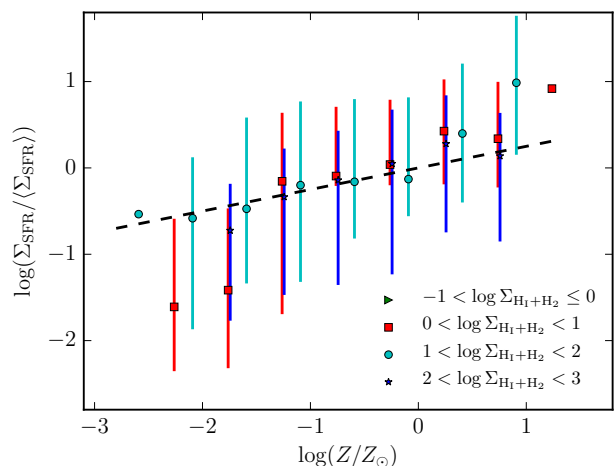


Figure 7. Star formation rate dependence on metallicity, binned by $\Sigma_{\text{HI}+\text{H}_2}$ at 1 kpc^2 pixel size. Points are average values of the 10 Myr-average Σ_{SFR} normalized by the average Σ_{SFR} in each $\Sigma_{\text{HI}+\text{H}_2}$ bin. Error bars denote the 5-95% range for resolved star formation in each bin. A weak dependence on metallicity is seen for all gas surface densities, as demonstrated by the dashed black line of slope $\Sigma_{\text{SFR}} \propto Z^{1/4}$.

Schmidt relation at moderately high surface density in the FIRE simulations. Remarkably – given the simplicity of the derivation – when Equation 7 is used on a pixel-by-pixel basis to predict star formation rates from $\Sigma_{\text{HI}+\text{H}_2}$ and Σ_{\star} , the predicted rates are nearly identical to the 10 Myr-averaged and instantaneous star formation rates, extending down to $\Sigma_{\text{HI}+\text{H}_2} \approx 10^{-1} \text{ M}_{\odot} \text{ pc}^{-2}$.

4.2 Low Gas Surface Density Regime

At the other extreme of galactic environments, we consider the low gas surface density regime in which gas is supported by thermal – rather than turbulent – pressure. We expect this transition to occur for $\Sigma_{\text{gas}} \lesssim 10 \text{ M}_{\odot} \text{ pc}^{-2}$; see Ostriker et al. (2010) and Hayward & Hopkins (2015) for details. In this regime, a star formation equilibrium rate can be derived by balancing photoheating from young stars with gas cooling. At extremely low gas surface densities, where $\Sigma_{\text{gas}} \ll 1 \text{ M}_{\odot} \text{ pc}^{-2}$, the metagalactic UV background itself may become the predominant source of heating, requiring no star formation at all to maintain a thermal pressure equilibrium (Ostriker et al. 2010).

As derived in Ostriker et al. (2010) as an “outer-disk” law, we can balance photoheating with radiative gas cooling. For ionizing and photo-electric photons dominating the gas heating, the heating rate per area is

$$\frac{\dot{E}_{\text{heat}}}{l^2} = \frac{f_{\text{abs}} \beta L_{\star}}{l^2} = f_{\text{abs}} \beta \epsilon c^2 \dot{\Sigma}_{\star}, \quad (8)$$

where $f_{\text{abs}} (\lesssim 1)$ is the fraction of the emitted photoheating photons absorbed by surrounding gas, $\beta \sim 0.1$ is the fraction of ionizing radiation emitted by young stars (Leitherer et al. 1999), and $\epsilon \sim 4 \times 10^{-4}$ is the fraction of rest-mass energy radiated by stars in their lifetimes. On the other hand, the cooling rate per area is

$$\frac{\dot{E}_{\text{cool}}}{l^2} = \frac{\Lambda n_e n_i V}{l^2} \approx \frac{\Lambda Z n_g \Sigma_{\text{gas}}}{\mu}, \quad (9)$$

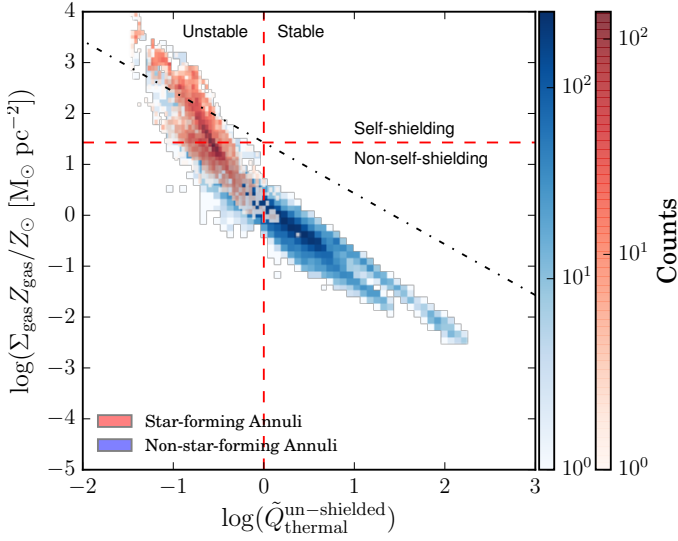


Figure 8. Comparison of whether self-shielding or gravitational instability determines the onset of efficient star formation (see §4.3). For each radial annulus in each galaxy (500 pc wide annuli, at each time from $z = 0.5 - 0$), we measure $\tilde{Q}_{\text{thermal}}^{\text{un-shielded}}$ (Eq. 13) and $\Sigma_{\text{gas}} Z_{\text{gas}} / Z_{\odot}$. We plot a heat map of the number of pixels with each value of $\tilde{Q}_{\text{thermal}}^{\text{un-shielded}}$ and $\Sigma_{\text{gas}} Z_{\text{gas}} / Z_{\odot}$, color-coded so star-forming annuli are red (mean $\dot{\Sigma}_{\star} > 10^{-3} \text{ M}_{\odot} \text{ kpc}^{-2} \text{ yr}^{-1}$) and non-star-forming annuli are blue. $\tilde{Q}_{\text{thermal}}^{\text{un-shielded}}$ is the Toomre- Q parameter if the gas were purely thermally supported with $T = 10^4 \text{ K}$; this indicates whether the gas could be thermally stabilized against gravitational instabilities if it were not self-shielding. $\Sigma_{\text{gas}} Z_{\text{gas}} / Z_{\odot}$ is a proxy for optical depth, approximating whether or not the gas is self-shielding to ionizing radiation. Vertical and horizontal dotted red lines indicate the $Q = 1$ stability threshold and the self-shielding threshold derived in Krumholz et al. (2009b), respectively. Black dotted line shows the track of varying Σ_{gas} at fixed Z' and Ω . The onset of star formation clearly occurs around $\tilde{Q}_{\text{thermal}}^{\text{un-shielded}} \sim 1$, even though the annuli are not self-shielding—i.e. gravitational instability initiates collapse, which then produces dense self-shielding clumps.

with $\Lambda \sim 10^{-22} \text{ erg s}^{-1} \text{ cm}^{-3}$ being the net cooling rate (Robertson & Kravtsov 2008); n_e , n_i , and n_g being the electron, ion, and gas number densities; and $V \sim l^2 h$ being the volume of gas considered. Equating the heating and cooling rates, we find

$$\dot{\Sigma}_{\star} \approx \frac{\Lambda Z n_g \Sigma_{\text{gas}}}{f_{\text{abs}} \mu \beta \epsilon c^2}. \quad (10)$$

Furthermore, we have $n_g = \rho_{\text{gas}} / \mu \approx \Sigma_{\text{gas}} / 2h\mu$ and $h \approx c_s / \Omega$ in the thermally supported limit, as $\sqrt{c_s^2 + \sigma_T^2} \approx c_s$. Thus, we have $n_g \approx \Sigma_{\text{gas}} \Omega / 2c_s \mu$, and $\dot{\Sigma}_{\star}$ becomes

$$\dot{\Sigma}_{\star} \approx \frac{\Lambda Z \Omega \Sigma_{\text{gas}}^2}{2 f_{\text{abs}} \mu^2 \beta \epsilon c^2 c_s} = \frac{\Sigma_0 Z \Omega}{f_{\text{abs}}} \left(\frac{\Sigma_{\text{gas}}}{\Sigma_0} \right)^2, \quad (11)$$

where $\Sigma_0 \approx 2\mu^2 \beta \epsilon c^2 c_s / \Lambda \approx 4 \text{ M}_{\odot} \text{ pc}^{-2}$, assuming $T = 10^4 \text{ K}$, for which $c_s \approx 12 \text{ km s}^{-1}$. Scaling this to approximately Milky-Way values ($\Omega \approx v_c / R \approx 220 \text{ km s}^{-1} / R$, $Z \approx Z_{\odot}$), we have

$$\dot{\Sigma}_{\star} \approx 1.3 \times 10^{-3} \left(\frac{Z}{Z_{\odot}} \right) \left(\frac{10 \text{ kpc}}{R} \right) \left(\frac{\Sigma_{\text{gas}}}{\Sigma_0} \right)^2 \frac{1}{f_{\text{abs}}} \text{ M}_{\odot} \text{ yr}^{-1} \text{ kpc}^{-2}. \quad (12)$$

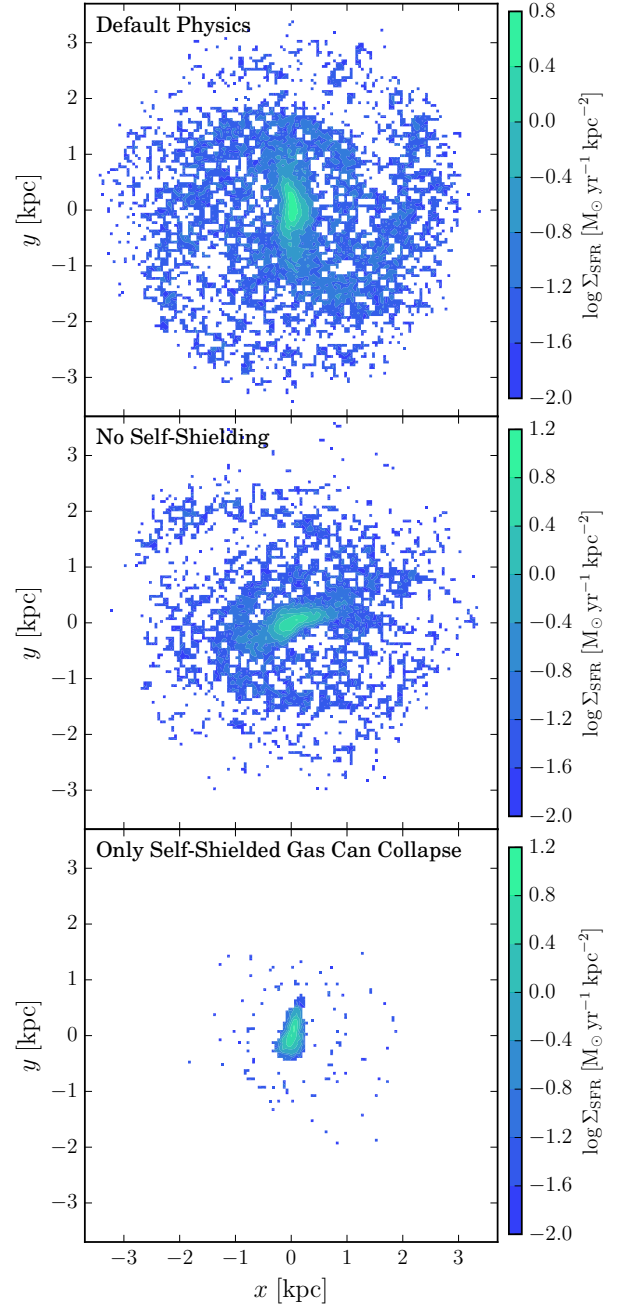


Figure 9. Demonstration of the importance of gravitational instability versus self-shielding in star formation. One Milky Way-mass simulation, **m12i** presented in Hopkins et al. (2014), was restarted from $z \approx 0.07$ and rerun with three sets of physics, the default physics implemented in the FIRE runs (**top**), one with both self-shielding and cooling below 10^4 K disabled (**middle**), and one where shielded gas had normal properties but non-shielded gas had a large artificial pressure floor, effectively disabling gravitational fragmentation until the gas first became self-shielding (**bottom**). Colored pixels indicate the extent and intensity of star formation since the runs were restarted in the form of the 500 Myr averaged star formation rate surface density. The star formation largely has the same structure with or without self-shielding, as long as fragmentation is allowed (gas can still isothermally collapse and meet the star formation criteria). But when only annuli in a galaxy which are entirely self-shielding can fragment or collapse, only the central $\sim \text{kpc}$ of the galaxy (where the gas is entirely molecular) efficiently forms stars.

The star formation rate relation for a thermally supported ISM has the same $\dot{\Sigma}_* \propto \Sigma_{\text{gas}}^2$ dependence as the turbulently supported high gas surface density regime when the gas surface density dominates, but with an added dependence on Z and Ω . This is similar to the relations found by Ostriker et al. (2010) and Krumholz et al. (2009b) at low surface densities, with their dependence on metallicity. The scaling here is in good agreement with the FIRE runs at low gas surface densities for the $\Sigma_{\text{HI}+\text{H}_2}$ tracer but differs from the shallower relations found by some observational studies (Bigiel et al. 2010; Roychowdhury et al. 2015). For low column densities, where $f_{\text{abs}} \ll 1$, the fraction of absorbed photoheating photons may go as the optical depth and thus the gas surface density $f_{\text{abs}} \propto (1 - \exp(-\tau)) \approx \tau \propto \Sigma_{\text{gas}} Z'$, reducing the low gas surface density relation to $\dot{\Sigma}_* \propto \Sigma_{\text{gas}}$, which may explain the aforementioned shallower observations. Similarly to the turbulently supported regime derivation, comparing the predictive ability of Equation 12 using pixel-by-pixel values of Z , Ω , and $\Sigma_{\text{HI}+\text{H}_2}$ with the measured star formation rates, very close agreement is found for $\Sigma_{\text{HI}+\text{H}_2} \lesssim 10 \text{ M}_\odot \text{ pc}^{-2}$, the regime in which the relation is expected to apply (Hayward & Hopkins 2015).

4.3 Star Formation Thresholds

There remains the question of what, physically, *fires* up star formation in the simulations in the first place. Figures 8 and 9 address this question.

Consider a radial annulus of a smooth gas disk at some large radius R . At sufficiently large R and low densities, the disk is not self-shielding to UV radiation, and even the meta-galactic UV background is sufficient to maintain the disk at warm temperatures $T \sim 10^4 \text{ K}$. The thermal Toomre- Q parameter at this temperature:

$$\tilde{Q}_{\text{thermal}}^{\text{un-shielded}} \equiv \frac{\kappa c_s (10^4 \text{ K})}{\pi G \Sigma_{\text{disk}}} \approx 0.7 \left(\frac{\Omega}{\text{Gyr}^{-1}} \right) \left(\frac{\text{M}_\odot \text{ pc}^{-2}}{\Sigma_{\text{disk}}} \right) \quad (13)$$

is $\tilde{Q}_{\text{thermal}}^{\text{un-shielded}} \gg 1$, i.e. the disk is fully stable. In this limit, we do not expect (nor see in our simulations) any significant star formation. In the opposite limit (in e.g. the centers of massive galaxies), the surface densities are high, $\tilde{Q}_{\text{thermal}}^{\text{un-shielded}} \ll 1$ (i.e. thermal support, even in the warm gas, is insufficient to stabilize the disk, so it is supersonically turbulent, with $Q \sim Q_{\text{turb}} \sim 1$) and the gas is self-shielding. In this limit, of course, we see efficient star formation.

What determines the transition between these two limits? It has been suggested that when an annulus reaches a critical column density to become self-shielding, it can suddenly cool to $T \ll 10^4 \text{ K}$, reducing the thermal pressure support of the gas disk against fragmentation (i.e. lowering the Toomre- Q from $\gg 1$ to $\ll 1$) and so initiating gravitational collapse and star formation (e.g. Schaye 2004; Krumholz et al. 2009a). This will occur when the dust optical depth $\tau = \Sigma_{\text{gas}} \kappa$ exceeds unity, or more accurately from Krumholz et al. (2009a), when $\Sigma_{\text{gas}} Z' > 27 \text{ M}_\odot \text{ pc}^{-2}$ (where $Z' \equiv Z/Z_\odot$ reflects the assumption of a constant dust-to-metals ratio).

Alternatively, an annulus which is *not* self-shielding (hence at a temperature $T \sim 10^4 \text{ K}$) will still become gravitationally unstable, when $\tilde{Q}_{\text{thermal}}^{\text{un-shielded}} \lesssim 1$, i.e.

$\Sigma_{\text{disk}} (\Omega/\text{Gyr}^{-1})^{-1} \gtrsim 0.7 \text{ M}_\odot \text{ pc}^{-2}$. The annulus would then rapidly fragment isothermally (at $\sim 10^4 \text{ K}$) at first, until individual overdensities/fragments quickly become internally self-shielding (reaching *local* surface densities $\Sigma_{\text{gas}} Z' > 27 \text{ M}_\odot \text{ pc}^{-2}$ as they collapse), then cool and fragment further to form stars. During this collapse, super-sonic turbulence would be driven by gravitational instabilities and feedback to maintain a turbulent $Q \sim 1$, but the important point is that the *thermal* support ($\tilde{Q}_{\text{thermal}}^{\text{un-shielded}}$) is insufficient.

The question is essentially which of these thresholds is reached “first.” Figure 8 examines this in our simulations by plotting all annuli in the space of $\tilde{Q}_{\text{thermal}}^{\text{un-shielded}} \propto \Omega/\Sigma_{\text{disk}}$ versus $\tau_{\text{shielding}} \propto \Sigma_{\text{gas}} Z$, and identifying those which are and are not star-forming. Clearly, robust star formation occurs in annuli which are not, on average, self-shielding (they have $\Sigma_{\text{gas}} Z' \approx 1 - 5 \text{ M}_\odot \text{ pc}^{-2}$). We stress that the small sub-regions where star-formation is occurring *within* those annuli are of course self-shielding (this is in fact required by our resolution-scale star formation model), and reach $\Sigma_{\text{gas}} Z' \gg 100 \text{ M}_\odot \text{ pc}^{-2}$ locally. In contrast, the onset of star formation corresponds very closely to where $\tilde{Q}_{\text{thermal}}^{\text{un-shielded}} \approx 1$. This is consistent with observations of star-forming spiral galaxies by Martin & Kennicutt (2001) who found that gravitational instability thresholds were sufficient to explain the extent of star-forming disks.

Examining Figure 8 further, we see that the annuli all lie on a track which intercepts the instability threshold $\tilde{Q}_{\text{thermal}}^{\text{un-shielded}} \approx 1$ more than a dex below the self-shielding threshold $\Sigma_{\text{gas}} Z' \sim 27 \text{ M}_\odot \text{ pc}^{-2}$. Star formation (red pixels) is seen as annuli cross the instability line, and the distribution then turns upwards as star formation begins to enrich the annuli in Z' without much affecting Σ_{gas} or $\tilde{Q}_{\text{thermal}}^{\text{un-shielded}}$ instantaneously. As annuli cross into the self-shielding regime, Σ_{gas} quickly crosses into the high surface density regime, and vigorous star formation results in short depletion timescales for these annuli, preventing highly shielded, low- $\tilde{Q}_{\text{thermal}}^{\text{un-shielded}}$ annuli from remaining long in that regime. Crossing into the self-shielded regime appears to coincide with the rapid rise in the lower envelope of $\dot{\Sigma}_*$ – these regions are vigorously forming stars throughout and are unable to prevent themselves from cooling rapidly and fragmenting, as in Schaye (2004). Moreover, the high- $\tilde{Q}_{\text{thermal}}^{\text{un-shielded}} \gg 10$ annuli with very low $\Sigma_{\text{gas}} Z'$ appear to come from the galactic outskirts at several times the half-mass radii.

To verify the relative importance of gravitational instability versus self-shielding, we also considered an idealized numerical experiment in Figure 9. Specifically, we took one of our Milky Way-mass galaxy simulations (run **m12i** from Hopkins et al. 2014) and re-ran it for about $\sim 1 \text{ Gyr}$ close to $z = 0$ (from $z = 0.07$ to $z = 0$), modifying the physics in the re-run. We considered two cases.

- (1) “No Self-Shielding:” In this case we disable self-shielding in our radiative heating routines and do not allow any cooling below 10^4 K .⁶ Clearly, Figure 9 shows that gas is still able to fragment and form stars – the spatial extent of

⁶ In our “no self-shielding” run, we still enforce the Krumholz & Gnedin (2011) requirement described in § 2 for whether an individual gas particle is allowed to form stars, since this is (strictly speaking) just a metallicity-dependent *local* surface den-

the star formation is nearly identical to our “default” run, in fact, indicating that cooling to $T \ll 10^4$ K is not what determines the outer cutoff of star formation in the disk (consistent with our argument in Figure 8). The total star formation rate is also similar within 15%.

- (2) “Only Self-Shielded Gas Can Collapse:” If self-shielding always preceded fragmentation and star formation, we should be able to disable Toomre-style fragmentation in gas which is not self-shielding, and obtain the same result. This is non-trivial in practice. We attempt to implement this as follows: for gas which is self-shielding (has cooled to < 8000 K and/or meets the Krumholz & Gnedin (2011) criterion), the physics is “normal,” but for gas which is not self-shielding, we add an artificial pressure term to the hydrodynamic equations ($P \rightarrow P_{\text{true}} + P_{\text{floor}}$) where $P_{\text{floor}} = 4 \times 10^{-11} \text{ (n/cm}^{-3}\text{)}$ (i.e. the pressure the gas would have at 3×10^5 K). The specific value is chosen to ensure the non-shielded gas has an “effective” Toomre- $Q \sim$ a few (sufficient to prevent fragmentation but not “blow up” the galaxy). When we do this, we see that efficient star formation becomes restricted to the central $\sim \text{kpc}$ only (and the total star formation rate falls by a factor ≈ 3). This central region is basically the location of the molecular disk – i.e. the regime where the gas is *entirely* molecular, since that is where the disk is uniformly self-shielding. Clearly, this is not a good description of star formation in the “default” simulation.

4.3.1 Star Formation in the Small Magellanic Cloud

The star formation threshold behavior seen in our simulations is consistent with observations of the Small Magellanic Cloud (SMC). The star formation rates seen by Hony et al. (2015) agree well with the spatially resolved Kennicutt-Schmidt relation when considering young star counts as a measure of $\dot{\Sigma}_*$. Moreover, considering the metallicity and surface density of the SMC, in the SMC body/wing, $\tau \sim \Sigma_{\text{gas}} Z / Z_{\odot} \sim 10 \text{ M}_{\odot} \text{ pc}^{-2}$, and in the SMC tail, $\Sigma_{\text{gas}} Z / Z_{\odot} \sim 2 \text{ M}_{\odot} \text{ pc}^{-2}$ (Oliveira 2009; Nidever et al. 2008), the SMC body is thus not quite at the self-shielding threshold, and the tail is certainly not. On the other hand, when estimating Q for the SMC wing, one finds $Q \sim 2/3$ and for the body $Q \ll 1$ (assuming a linearly rising rotation curve to $v_{\text{rot}} \sim 50 \text{ km s}^{-1}$ at $R \sim 3.5 \text{ kpc}$ found by Stanimirović et al. (2004)); hence, the SMC appears to be consistent with gravitational instabilities triggering star formation.

5 CONCLUSIONS

In this paper, we investigated the spatially-resolved Kennicutt-Schmidt relation in the cosmological FIRE simulations with $z = 0$ central halo masses ranging from $10^{10} \text{ M}_{\odot}$ to $10^{13} \text{ M}_{\odot}$. In the FIRE simulations, star formation occurs with an instantaneous efficiency of 100% per free fall time in dense, locally self-gravitating, molecular gas clumps. However, star formation is inefficient on galactic scales – in agreement with observed Kennicutt-Schmidt relations – thanks to

sity threshold ($\Sigma_{\text{gas}} Z' > 27 \text{ M}_{\odot} \text{ pc}^{-2}$) evaluated at the resolution scale.

a global balance between gravity and stellar feedback. This is true across many orders of magnitude in halo mass and at all redshifts studied. The exact slope of the relationship between Σ_{SFR} and Σ_{gas} depends on the gas and star formation tracers used, but the two quantities are tightly correlated in all cases explored.

Our main findings are as follows:

- The time-averaged Kennicutt-Schmidt relation does not appear to have a significant dependence on pixel size (i.e. map resolution) for gas surface densities with sufficiently resolved star formation rate distributions (i.e. above the Σ_{gas} where the KS relation would yield at least a few young star particles per pixel given our mass resolution, c.f. §2), with the slope of the power law remaining effectively unchanged. However, we are unable to resolve star formation rates at gas surface densities at our smallest pixel size (100 pc) for which observations exhibited large scatter in the Kennicutt-Schmidt relation ($\Sigma_{\text{gas}} \lesssim 10 \text{ M}_{\odot} \text{ pc}^{-2}$).

- The Kennicutt-Schmidt relation in the FIRE simulations is independent of redshift. The simulations do not exhibit any metallicity-dependent cutoff; however, the star formation rate surface density is weakly dependent on the metallicity, on the order expected from SNe feedback’s momentum injection dependence on metallicity (Cioffi et al. 1988; Martizzi et al. 2015).

- At the high end of gas surface density, where $\Sigma_{\text{gas}} \gtrsim 100 \text{ M}_{\odot} \text{ pc}^{-2}$ and gas is predominantly molecular, we find that the Kennicutt-Schmidt relation obeyed by the simulated galaxies is consistent with injection of momentum from supernovae balancing momentum dissipation in turbulence, or analogously, turbulent “pressure” maintaining vertical hydrostatic equilibrium (Ostriker & Shetty 2011; Faucher-Giguère et al. 2013; Hayward & Hopkins 2015). This explanation yields a power law independent of redshift or metallicity at high gas surface densities, where $\dot{\Sigma}_* \propto \Sigma_{\text{gas}} \Sigma_{\text{disk}}$. Because the disks in our simulations are not particularly gas rich, we find a slightly steeper than linear Kennicutt-Schmidt relation in this regime.

- In regions of low gas surface density ($\Sigma_{\text{gas}} \lesssim 10 \text{ M}_{\odot} \text{ pc}^{-2}$), characteristically in galaxy outskirts and regions between spiral arms, our spatially-resolved Kennicutt-Schmidt relation agrees well with that expected from a simple local equilibrium between photoheating from ionizing, or near-ionizing, radiation from young stars and radiative gas cooling. This argument yields a $\dot{\Sigma}_* \propto Z \Sigma_{\text{gas}}^2$ power law, as discussed in Ostriker et al. (2010) and Hayward & Hopkins (2015).

- Vigorous star formation begins as gas self-gravity overcomes the gas thermal pressure gradient, thus making the gas Toomre-unstable. This self-gravity driven collapse occurs at $\Sigma_{\text{gas}} \sim 1 \text{ M}_{\odot} \text{ pc}^{-2}$, an order of magnitude before the gas becomes self-shielding to UV radiation, at $\Sigma_{\text{gas}} \sim 27 \text{ M}_{\odot} \text{ pc}^{-2}$. Thus, we find that in the FIRE simulations, star formation is triggered by gravitational instabilities, which then cause the gas to fragment and collapse, thereby becoming self-shielding to ionizing radiation, cooling rapidly and forming stars. The threshold for gravitational instability, $Q \sim \Omega / \Sigma_{\text{disk}}$, depends only on the density of gas and stars, i.e. the criterion for warm gas ($T \gtrsim 10^4$ K) to support itself thermally against fragmentation, and subsequently star formation, is independent of both Z and z .

Future observations with high spatial resolution and sensitivity to low surface brightnesses should aid in understanding the outskirts of galactic environments where star formation is on the brink of *firing* up and the surface densities of gas and stars are near the thresholds of gravitational instability and self-shielding. This will help determine if gravitational fragmentation – rather than self-shielding – is indeed the primary triggering mechanism of star formation.

ACKNOWLEDGMENTS

MEO is grateful for the encouragement of his late father, SRO, in studying astrophysics, and for many helpful discussions with A. Wetzel. This research has made use of NASA’s Astrophysics Data System. This material is based upon work supported by the National Science Foundation Graduate Research Fellowship under Grant No. 1144469. CCH is grateful to the Gordon and Betty Moore Foundation for financial support. The Flatiron Institute is supported by the Simons Foundation. Support for PFH was provided by an Alfred P. Sloan Research Fellowship, NASA ATP Grant NNX14AH35G, and NSF Collaborative Research Grant #1411920 and CAREER grant #1455342. Numerical calculations were run on the Caltech compute cluster “Zwicky” (NSF MRI award #PHY-0960291) and allocations TG-AST120025, and TG-AST130039 granted by the Extreme Science and Engineering Discovery Environment (XSEDE) supported by the NSF. CAFG was supported by NSF through grants AST-1412836 and AST-1517491, by NASA through grant NNX15AB22G, and by STScI through grants HST-AR-14293.001-A and HST-GO-14268.022-A. DK acknowledges support from the NSF grant AST-1412153 and Cottrell Scholar Award from the Research Corporation for Science Advancement. EQ was supported by NASA ATP grant 12-ATP12-0183, a Simons Investigator award from the Simons Foundation, and the David and Lucile Packard Foundation.

REFERENCES

- Agertz O., Kravtsov A. V., 2015, preprint, ([arXiv:1509.00853](https://arxiv.org/abs/1509.00853))
- Agertz O., Kravtsov A. V., Leitner S. N., Gnedin N. Y., 2013, *ApJ*, **770**, 25
- Asplund M., Grevesse N., Sauval A. J., Scott P., 2009, *ARA&A*, **47**, 481
- Becerra F., Escala A., 2014, *ApJ*, **786**, 56
- Bigiel F., Leroy A., Walter F., Brinks E., de Blok W. J. G., Madore B., Thornley M. D., 2008, *AJ*, **136**, 2846
- Bigiel F., Leroy A., Walter F., Blitz L., Brinks E., de Blok W. J. G., Madore B., 2010, *AJ*, **140**, 1194
- Boquien M., Lisenfeld U., Duc P.-A., Braine J., Bournaud F., Brinks E., Charmandaris V., 2011, *A&A*, **533**, A19
- Bothwell M. S., et al., 2010, *MNRAS*, **405**, 219
- Bouché N., et al., 2007, *ApJ*, **671**, 303
- Calzetti D., Liu G., Koda J., 2012, *ApJ*, **752**, 98
- Chan T. K., Kereš D., Oñorbe J., Hopkins P. F., Muratov A. L., Faucher-Giguère C.-A., Quataert E., 2015, *MNRAS*, **454**, 2981
- Cioffi D. F., McKee C. F., Bertschinger E., 1988, *ApJ*, **334**, 252
- Daddi E., et al., 2010, *ApJ*, **714**, L118
- Elmegreen B. G., 1997, in Franco J., Terlevich R., Serrano A., eds, *Revista Mexicana de Astronomía y Astrofísica*, vol. 27 Vol. 6, Revista Mexicana de Astronomía y Astrofísica Conference Series. p. 165
- Faucher-Giguère C.-A., Quataert E., Hopkins P. F., 2013, *MNRAS*, **433**, 1970
- Federrath C., Klessen R. S., 2012, *ApJ*, **761**, 156
- Feldmann R., Gnedin N. Y., 2011, *ApJ*, **727**, L12
- Feldmann R., Gnedin N. Y., Kravtsov A. V., 2011, *ApJ*, **732**, 115
- Feldmann R., Gnedin N. Y., Kravtsov A. V., 2012, *ApJ*, **758**, 127
- Feldmann R., Hopkins P. F., Quataert E., Faucher-Giguère C.-A., Kereš D., 2016, *MNRAS*, **458**, L14
- Freundlich J., et al., 2013, *A&A*, **553**, A130
- Genzel R., et al., 2010, *MNRAS*, **407**, 2091
- Glover S. C. O., Clark P. C., 2012, *MNRAS*, **421**, 9
- Gnedin N. Y., Kravtsov A. V., 2011, *ApJ*, **728**, 88
- Gnedin N. Y., Tasker E. J., Fujimoto Y., 2014, *ApJ*, **787**, L7
- Hayward C. C., Hopkins P. F., 2015, preprint, ([arXiv:1510.05650](https://arxiv.org/abs/1510.05650))
- Hayward C. C., et al., 2014, *MNRAS*, **445**, 1598
- Hollenbach D. J., Tielens A. G. G. M., 1999, *Reviews of Modern Physics*, **71**, 173
- Hony S., et al., 2015, *MNRAS*, **448**, 1847
- Hopkins P. F., 2013, *MNRAS*, **428**, 2840
- Hopkins P. F., Quataert E., Murray N., 2011, *MNRAS*, **417**, 950
- Hopkins P. F., Quataert E., Murray N., 2012a, *MNRAS*, **421**, 3488
- Hopkins P. F., Quataert E., Murray N., 2012b, *MNRAS*, **421**, 3522
- Hopkins P. F., Cox T. J., Hernquist L., Narayanan D., Hayward C. C., Murray N., 2013a, *MNRAS*, **430**, 1901
- Hopkins P. F., Narayanan D., Murray N., 2013b, *MNRAS*, **432**, 2647
- Hopkins P. F., Kereš D., Murray N., Hernquist L., Narayanan D., Hayward C. C., 2013c, *MNRAS*, **433**, 78
- Hopkins P. F., Kereš D., Oñorbe J., Faucher-Giguère C.-A., Quataert E., Murray N., Bullock J. S., 2014, *MNRAS*, **445**, 581
- Hopkins P. F., Torrey P., Faucher-Giguère C.-A., Quataert E., Murray N., 2016, *MNRAS*, **458**, 816
- Kennicutt Jr. R. C., 1998, *ApJ*, **498**, 541
- Kennicutt R. C., Evans N. J., 2012, *ARA&A*, **50**, 531
- Kennicutt Jr. R. C., et al., 2007, *ApJ*, **671**, 333
- Kim C.-G., Ostriker E. C., 2015, *ApJ*, **802**, 99
- Kroupa P., 2002, *Science*, **295**, 82
- Kruijssen J. M. D., Longmore S. N., 2014, *MNRAS*, **439**, 3239
- Krumholz M. R., Gnedin N. Y., 2011, *ApJ*, **729**, 36
- Krumholz M. R., Tan J. C., 2007, *ApJ*, **654**, 304
- Krumholz M. R., Thompson T. A., 2007, *ApJ*, **669**, 289
- Krumholz M. R., McKee C. F., Tumlinson J., 2009a, *ApJ*, **693**, 216
- Krumholz M. R., McKee C. F., Tumlinson J., 2009b, *ApJ*, **699**, 850
- Leitherer C., et al., 1999, *ApJS*, **123**, 3
- Lisenfeld U., et al., 2011, *A&A*, **534**, A102
- Liu G., Koda J., Calzetti D., Fukuhara M., Momose R., 2011, *ApJ*, **735**, 63
- Martin C. L., Kennicutt Jr. R. C., 2001, *ApJ*, **555**, 301
- Martizzi D., Faucher-Giguère C.-A., Quataert E., 2015, *MNRAS*, **450**, 504
- Martizzi D., Fielding D., Faucher-Giguère C.-A., Quataert E., 2016, *MNRAS*, **459**, 2311
- Mihos J. C., Hernquist L., 1994, *ApJ*, **437**, 611
- Murray N., 2011, *ApJ*, **729**, 133
- Murray N., Quataert E., Thompson T. A., 2010, *ApJ*, **709**, 191
- Narayanan D., Krumholz M. R., Ostriker E. C., Hernquist L., 2012, *MNRAS*, **421**, 3127
- Nidever D. L., Majewski S. R., Butler Burton W., 2008, *ApJ*, **679**, 432

- Oliveira J. M., 2009, in Van Loon J. T., Oliveira J. M., eds, IAU Symposium Vol. 256, The Magellanic System: Stars, Gas, and Galaxies. pp 191–202 ([arXiv:0812.2360](#)), [doi:10.1017/S1743921308028457](#)
- Onodera S., et al., 2010, *ApJ*, **722**, L127
- Ostriker E. C., Shetty R., 2011, *ApJ*, **731**, 41
- Ostriker E. C., McKee C. F., Leroy A. K., 2010, *ApJ*, **721**, 975
- Padoan P., 1995, *MNRAS*, **277**, 377
- Papadopoulos P. P., Pelupessy F. I., 2010, *ApJ*, **717**, 1037
- Rafelski M., Gardner J. P., Fumagalli M., Neeleman M., Teplitz H. I., Grogin N., Koekemoer A. M., Scarlata C., 2016, *ApJ*, **825**, 87
- Robertson B. E., Kravtsov A. V., 2008, *ApJ*, **680**, 1083
- Rownd B. K., Young J. S., 1999, *AJ*, **118**, 670
- Roychowdhury S., Huang M.-L., Kauffmann G., Wang J., Chhengalur J. N., 2015, *MNRAS*, **449**, 3700
- Saitoh T. R., Daisaka H., Kokubo E., Makino J., Okamoto T., Tomisaka K., Wada K., Yoshida N., 2008, *PASJ*, **60**, 667
- Schaye J., 2004, *ApJ*, **609**, 657
- Schaye J., Dalla Vecchia C., 2008, *MNRAS*, **383**, 1210
- Schmidt M., 1959, *ApJ*, **129**, 243
- Schruba A., Leroy A. K., Walter F., Sandstrom K., Rosolowsky E., 2010, *ApJ*, **722**, 1699
- Semenov V. A., Kravtsov A. V., Gnedin N. Y., 2016, *ApJ*, **826**, 200
- Shapiro K. L., et al., 2010, *MNRAS*, **402**, 2140
- Shetty R., Kelly B. C., Bigiel F., 2013, *MNRAS*, **430**, 288
- Shetty R., Kelly B. C., Rahman N., Bigiel F., Bolatto A. D., Clark P. C., Klessen R. S., Konstantin L. K., 2014a, *MNRAS*, **437**, L61
- Shetty R., Clark P. C., Klessen R. S., 2014b, *MNRAS*, **442**, 2208
- Shi Y., Helou G., Yan L., Armus L., Wu Y., Papovich C., Stierwalt S., 2011, *ApJ*, **733**, 87
- Silk J., 1997, *ApJ*, **481**, 703
- Sparre M., Hayward C. C., Feldmann R., Faucher-Giguère C.-A., Muratov A. L., Kereš D., Hopkins P. F., 2015, preprint, ([arXiv:1510.03869](#))
- Springel V., Hernquist L., 2003, *MNRAS*, **339**, 289
- Stanimirović S., Staveley-Smith L., Jones P. A., 2004, *ApJ*, **604**, 176
- Tacconi L. J., et al., 2013, *ApJ*, **768**, 74
- Thompson T. A., Quataert E., Murray N., 2005, *ApJ*, **630**, 167
- Toomre A., 1964, *ApJ*, **139**, 1217
- Torrey P., Hopkins P. F., Faucher-Giguère C.-A., Vogelsberger M., Quataert E., Kereš D., Murray N., 2016, preprint, ([arXiv:1601.07186](#))
- Verley S., Corbelli E., Giovanardi C., Hunt L. K., 2010, *A&A*, **510**, A64
- Wei L. H., Vogel S. N., Kannappan S. J., Baker A. J., Stark D. V., Laine S., 2010, *ApJ*, **725**, L62
- Williams J. P., McKee C. F., 1997, *ApJ*, **476**, 166
- Wong T., Blitz L., 2002, *ApJ*, **569**, 157

APPENDIX A: ROBUSTNESS OF STAR FORMATION RATES TO VARIATIONS IN STAR FORMATION, COOLING, AND STELLAR FEEDBACK

Here, we demonstrate the robustness of the star formation rate in the FIRE simulations to reasonable changes in the implemented star formation, cooling, and stellar feedback physics (reviewed in detail in [Hopkins et al. 2014](#)). A number of previous studies have consistently demonstrated the convergence of star formation rates and the Kennicutt-Schmidt relation, with resolution and numerical implementations of star formation ([Saitoh et al. 2008](#); [Federrath & Klessen 2012](#);

[Hopkins et al. 2012b, 2013c,a,b, 2016](#); [Agertz et al. 2013](#)). In Figure A1, we illustrate this with a set of simple tests (part of a more general numerical study, which will be presented in detail in [Hopkins et al. 2017](#) (in prep)). In each case, we re-start the same Milky-Way mass simulation (**m12i** from [Hopkins et al. \(2014\)](#) as in §4.3 in the text), and re-run it from $z = 0.07 - 0$ with different numerical choices. This ensures the initial conditions are identical; Σ_{gas} for the galaxy, for example, is fixed, so we can simply read off from the star formation rate whether the galaxy’s location in the Kennicutt-Schmidt law would change.

We compare our default star formation model, using the criteria enumerated in §2 with $n_{\text{crit}} = 50 \text{ cm}^{-3}$ and $\epsilon_{\text{sf}} = 1$, where ϵ_{sf} represents the local efficiency with which gas turns into stars in a free fall time, i.e. $\dot{\rho}_{\star} = \epsilon_{\text{sf}} \rho_{\text{mol}} / t_{\text{ff}}$, to variations with $\epsilon_{\text{sf}} = 0.01 - 100$, $n_{\text{crit}} = 5 - 1000 \text{ cm}^{-3}$, and turning on/off the additional virial and molecular criteria. We find that the star formation rate (and indeed the entire spatially-resolved Kennicutt-Schmidt relation) is effectively the same in all cases.

We also vary our cooling model, replacing all low-temperature cooling physics with a single cooling rate, putting all gas on a single, solar-metallicity cooling curve, and removing the molecular star formation requirement. We see that there is no effect on the star formation rate; we similarly find no effect on the outflow rate or global morphology. Details of the phase structure, of course, differ, but these have no *large dynamical effect*, consistent with various previous studies that have found that almost all gas in galaxies is super-sonically turbulent and has cooling times much shorter than their dynamical times ([Hopkins et al. 2011, 2012a](#); [Glover & Clark 2012](#)).

We also explicitly consider the mass resolution convergence by up- and down-sampling the particle distribution with particle splitting/merging. We find that the star formation rate is nearly identical over ~ 2.5 dex in mass resolution, even a factor of ~ 10 lower resolution compared to our “standard FIRE” resolution. This is consistent with our argument in §2 that we only need to marginally resolve the Toomre scale to achieve convergence in the star formation rate because the most massive clouds dominate star formation ([Williams & McKee 1997](#)).

As seen in the bottom left panel of Figure A1, variation in the strength of feedback per mass of young stars is the only effective means of changing the star formation rate. As galaxies self-regulate for a given level of feedback, changing the strength of feedback systematically results in higher star formation rates for lower levels of feedback per star and vice versa. This is consistent with our scalings in §4.

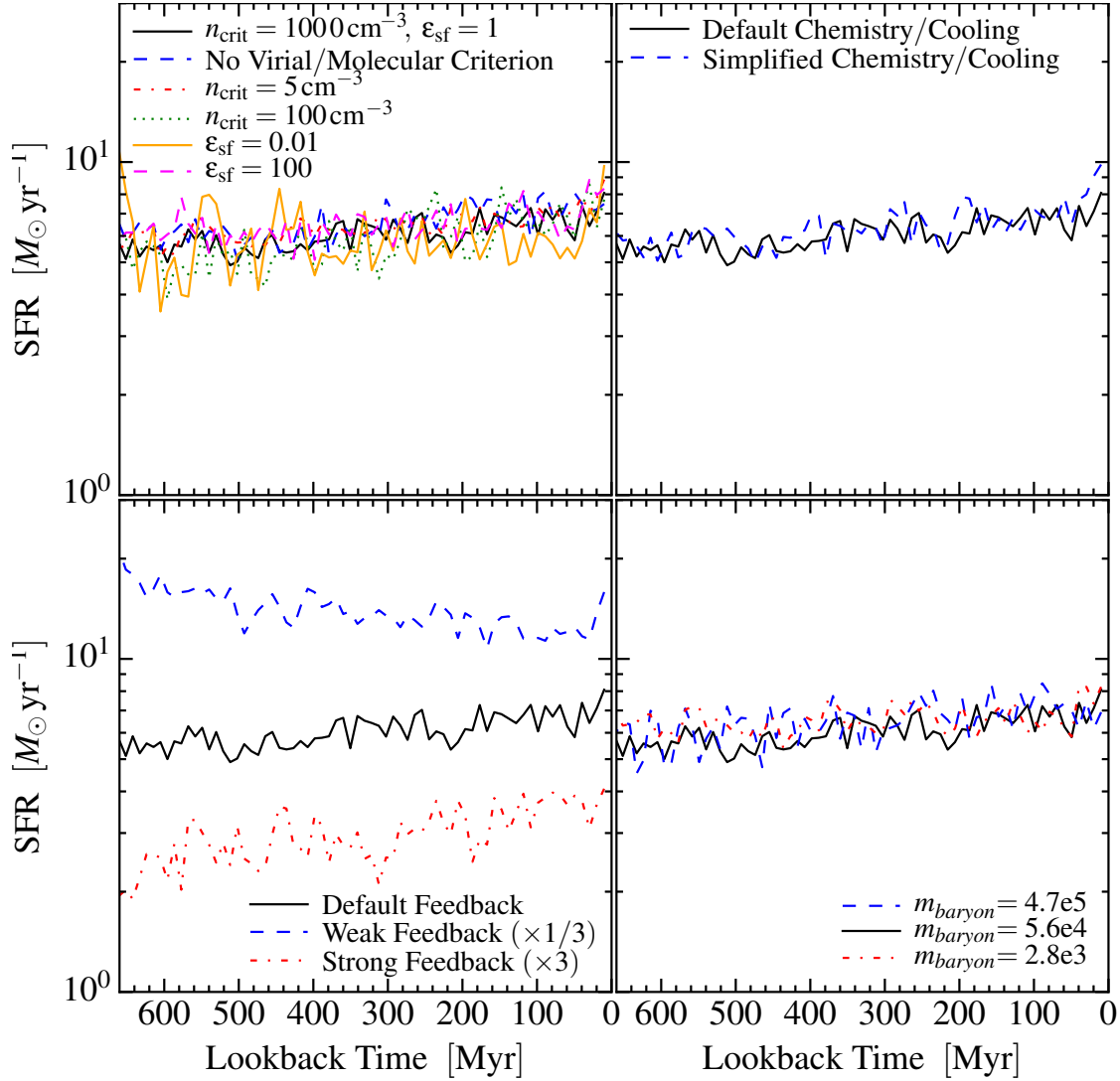


Figure A1. Star formation rate versus time in our MW-mass (**m12i**) simulation from redshift $z \approx 0.07 - 0$; the simulation was restarted at $z = 0.07$ and run with varying parameters to study the effect on the star formation rate given the same initial galaxy properties. **Top Left:** Effect of the resolution-scale star formation criteria. In our “default” model, gas that is self-gravitating, molecular, and dense ($n > n_{\text{crit}} = 1000 \text{ cm}^{-3}$) forms stars at a rate $\dot{\rho} = \epsilon_{\text{sf}} \rho_{\text{mol}}/t_{\text{ff}}$, with $\epsilon_{\text{sf}} = 1$. We compare (1) removing the self-gravity & molecular restrictions, (2-3) varying n_{crit} , and (4-5) varying ϵ_{sf} . **Bottom Left:** We vary the strength of feedback by multiplying/dividing the rates of all mechanisms per unit stellar mass by 3 relative to the predictions from the stellar evolution models. **Top Right:** Default physical cooling model compared with a toy model that ignores all low-temperature cooling physics and puts all gas on a single, solar-metallicity cooling curve. **Bottom Right:** Resolution effects, changing the baryonic particle mass. The results of this figure show that only the strength of feedback significantly alters the star formation rate at fixed Σ_{gas} , varying the sub-grid star formation law has essentially no effect.